Inorganic Chemistry

pubs.acs.org/IC Article

NaW_2S_4 and Rb_xWS_2: Alternative Sources for 2M-WS_2 and 1T′-WS_2 Monolayers

Brianna L. Hoff, Grigorii Skorupskii, Jaime M. Moya, Fang Yuan, Guangming Cheng, Jiaze Xie, Nan Yao, and Leslie M. Schoop*

Cite This: *Inorg. Chem.* 2024, 63, 21954−21962 Read Online

ACCESS | Metrics & More | Article Recommendations | Supporting Information

ABSTRACT: With the recent strive to develop novel quantum materials, including two-dimensional nanosheets, alkali-layered intercalated materials have found a new purpose as starting materials for such compounds. Enriching the library of alkali materials, we present a solid-state synthesis for preparing NaW_2S_4 ($P\bar{1}$, No. 2) and Rb_xWS_2 ($C2/m$, No. 12). Solving their crystal structure from their powder X-ray diffraction patterns, we show that both materials are layered, the former being a slightly distorted version of the latter. We compare the two structures and find that the main difference is the interlayer spacing in the a-direction. We further show that, like their cousin, K_xWS_2, both compounds can be deintercalated with dilute acid to form superconducting 2M-WS_2, with structural and property characterization showing similar behavior, regardless of the starting material. Lastly, we find that both materials can be exfoliated in the same manner as K_xWS_2 to form superconducting 1T′-WS_2 monolayers. We describe an easy one-step method for preparing two new layered materials and, thus, provide more opportunities to access valuable superconducting materials.

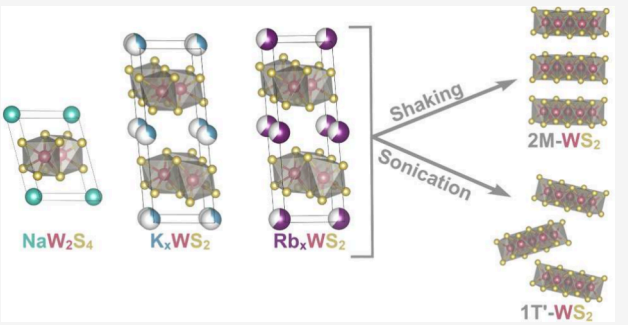

INTRODUCTION

For over four decades, alkali-layered intercalated materials (alkali-LIMs) have led to substantial breakthroughs in battery technology,[1,2] yet alkali-ion (de)intercalation of these layered materials has proven useful beyond electrochemical applications. A recent resurgence of interest in these materials stems from their use as precursors for accessing other—possibly otherwise unobtainable—compounds. Alkali layered materials can be deintercalated to obtain new metastable compounds, including superconducting FeS prepared from $K_xFe_{2-y}S_2$,[3] ferromagnetic 1T-$CrTe_2$ from $KCrTe_2$,[4] and antiferromagnetic 1T-$CrSe_2$ from $KCrSe_2$,[5,6] to name a few. The aforementioned metastable compounds cannot be prepared with solid-state reactions since the required high temperatures would result in the formation of alternative, thermodynamically stable phases. It should be noted, however, that there are other low-temperature methods capable of achieving metastable phases. Such is the case with tetragonal FeS (Mackinawite), which, owing to its promise for having superconductivity,[7,8] gained considerable interest in developing synthesis techniques. Among these, solvothermal synthesis starting with Fe and S[8] and solution synthesis with Fe and Na_2S[9] effectively produced tetrahedral FeS, but the resulting compounds did not demonstrate superconductivity. Lai et al. prepared the first superconducting polycrystalline FeS,[10] but it was through the treatment of $K_xFe_{2-y}S_2$ to remove K^+ that single crystals of superconducting FeS could be prepared.[3] Deintercalation of alkali metals from their original layered structure has also introduced novel materials with unique properties from their parent compound. Such is the case when Na^+ is partially deintercalated from $NaCoO_2$, yielding superconducting $Na_xCoO_2{\cdot}yH_2O$ compounds, with T_c dependent on the value of x.[11,12]

Alkali-LIMs can also be used as starting materials for chemically exfoliating into nanosheets. For example, MnO_2 monolayers have been prepared from $K_{0.45}MnO_2$,[13] $KFeS_2$ nanoribbons from bulk $KFeS_2$,[14] h-phase monolayers of RuO_2 were exfoliated from $K_{0.25}RuO_2$,[15] and IrOOH nanosheets were prepared from $K_{0.75}Na_{0.25}IrO_2$.[16] This method provides an advantage over other chemical exfoliation techniques in that it eliminates the need for possibly contaminating intercalating agents (i.e., *n*-butyl lithium or sodium napthalenide). Instead, it utilizes proton exchange to remove the intercalated ions, while osmotic swelling between the layers weakens the interlayer bonding; subsequent mechanical force is used to aid delamination.[17] Examples of this include Ti_3O_7 nanosheets formed from $Na_2Ti_3O_7$,[18] CoO_2

Received: August 6, 2024
Revised: October 8, 2024
Accepted: October 23, 2024
Published: November 5, 2024

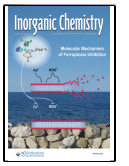

from $NaCoO_2$,[19] and titanate nanosheets from Cs-titanate.[20] This type of exfoliation will usually employ bulky intercalants (i.e., tetrabutylammonium hydroxide (TBAOH)), which may likewise leave a residue on the surface of the formed nanosheets. Instead, using redox chemistry, typically reserved for van der Waals layered materials, the alkali metal can be removed via an oxidative process while H_2 bubbles, formed during the process, force the layers apart.[21−23]

Recent work found that by treating one such alkali-LIM, K_xWS_2, with dilute acid, either superconducting bulk 2M-WS_2 crystals or superconducting 1T′-WS_2 monolayers can be prepared, depending on the specific acid concentration and concurrent mechanical force.[24−26] The former currently has one of the highest superconducting temperatures (T_c = 8.8 K) of any homogeneous transition metal dichalcogenide at ambient pressure.[27,28] The latter can be made into an ink, enabling it to be easily distributed onto devices of different textures. Furthermore, unlike typical deintercalation reactions, K^+ is fully removed from K_xWS_2 without proton exchange. Instead, the compound is oxidized, and H_2 gas formed during the process weakens the interlayer bonding, while ultrasonication fully separates the layers; H_2 gas formation eliminates the need for bulky intercalates typically required for osmotic swelling.

Finding new alkali-LIMs is incredibly important for advancing the field of materials science, both through direct applications and as a stepping-stone for increasing the library of available metastable compounds. Since the advent of the $LiCoO_2$ cathode in 1980, developing new layered materials capable of reaching higher capacity, higher energy density, and longer cycle life has been an ongoing concern. Recently, cost and safety concerns have put significant focus on replacing Li^+ with other intercalated ions. Such research is not as simple as merely replacing the alkali intercalant and assuming similar performance, since size differences may change the structure, stability, and (de)intercalation kinetics. A study conducted by Kaufman et al. found that Li^+ was too small to occupy the trigonal prismatic sites of a P3 layered structure of AMX_2 (A = alkali metal, M = transition metal, X = chalcogenide) since the X anions of neighboring layers would be too close to each other; Na^+ and K^+ were, however, large enough to keep the layers sufficiently far apart.[29] $LiTiS_2$ adopts the O1 layered structure, whereas Na_yTiS_2 prefers the O3 layered structure when concentrations of Na are high and the P3 layered structure when $y < 0.72$. Differences also persist in the electrochemical deintercalation process, where both $NaCoO_2$ and $KCoO_2$ were found to undergo multiple structural changes corresponding to the loss of alkali ions. Meanwhile, Yohannen et al. demonstrated the structural changes for $AInM'S_4$ (A = alkali, M′ = Ge, Sn) compounds.[30] For example, the $AInSnS_4$ family takes on different structures depending on the identity of A. When A = Na or K, it exhibits a hexagonal layered structure, whereas $LiInSnS_4$ takes on a cubic spinel structure.[30] Conversely, when A = Rb or Cs, $AInSnS_4$ can take on either a cubic structure (thermodynamically favorable) or an orthorhombic layered structure (kinetically favorable).[31] Therefore, despite being compositionally similar, substituting different alkali metals in $AInSnS_4$ yields different structures, lending themselves to different applications.

In this paper, we describe two new AWS_2-type compounds: NaW_2S_4 and Rb_xWS_2. We developed a one-step solid-state synthesis for preparing Na_xWS_2 ($P\bar{1}$, No. 2) and Rb_xWS_2 ($C2/m$, No. 12) from their respective elements. The Rb_xWS_2 that we synthesized here differs from the previously reported $Rb_{0.34}WS_2$ ($P2_1/m$, No. 11).[32] Furthermore, our sample preparation follows a straightforward, one-step method that involves heating the constituent elements in a furnace, unlike the previously reported synthesis, which required first preparing Rb_2S_2 by reacting Rb and S in liquid NH_3,[32] a relatively hazardous process. Therefore, we feel that, to the best of our knowledge, we have developed a simple method for making two novel materials; we do, however, acknowledge that caution must be taken when working with any alkali metal, as they are highly reactive. The structures of both NaW_2S_4 and Rb_xWS_2 were solved with TOPAS V7 (Bruker AXS) from their respective powder X-ray diffraction (PXRD) patterns. Our structure findings were further supported by high-resolution scanning/transmission electron microscopy (HRSTEM) images and selected area electron diffraction (SAED). We show that, as with K_xWS_2,[26] the alkali ion can be deintercalated from both compounds to form superconducting 2M-WS_2, which we confirm with magnetic susceptibility and heat capacity to have bulk superconductivity. Likewise, both compounds can be chemically exfoliated, like K_xWS_2,[25] to form monolayer 1T′-WS_2. We confirm the structure with Raman spectroscopy and the thickness with atomic force microscopy (AFM). The work we present here introduces compounds to the library of alkali-LIMs, which could potentially increase the accessibility of important metastable compounds, while simultaneously demonstrating a simple synthesis method that could be used to further prepare new alkali-LIMs.

EXPERIMENTAL SECTION

Preparation of Na_xWS_2. Polycrystalline Na_xWS_2 was prepared via a solid-state reaction. Stoichiometric ratios of Na (Sigma-Aldrich, 99.9%), W (Alfa Aesar, ≥ 99.9%), and S (Alfa Aesar, 99.5%) were placed in an alumina crucible and sealed under vacuum in a silica glass tube. The tube was then heated in a box furnace at a rate of 25 °C/h to 850 °C, where it dwelled for 72 h. It was then cooled at 3 °C/h to 550° before being shut off and allowed to cool to room temperature. The resulting black powder was stored in an argon glovebox to prevent hydration. Since the occupancy of Na was 1, making $x = 0.5$, we will refer to this compound as NaW_2S_4 for the rest of this paper.

Preparation of Rb_xWS_2. Polycrystalline Rb_xWS_2 was also prepared via a solid-state reaction. A 1:1:1 ratio of Rb (Sigma-Aldrich, 99.6%), W (Alfa Aesar, ≥ 99.9%), and S (Alfa Aesar, 99.5%) were placed in a graphite crucible and sealed under vacuum in a silica glass tube. The tube was then heated in a box furnace at a rate of 25 °C/h to 850 °C, where it dwelled for 48 h. It was then cooled at 3 °C/h to 550° before being shut off and allowed to cool to room temperature. The resulting Rb_xWS_2 crystals were sorted from powdered impurities and stored in an argon glovebox to prevent hydration.

Attempted Synthesis of Li_xWS_2. Attempted synthesis of Li_xWS_2 was prepared by combining stoichiometric ratios of Li (Sigma-Aldrich, 99%), W (Alfa Aesar, ≥ 99.9%), and S (Alfa Aesar, 99.5%) and following the same handling and heating profile as used for NaW_2S_4. An additional synthesis was carried out using stoichiometric ratios of Li_2S (Alfa Aesar, 99.9%), W (Alfa Aesar, ≥ 99.9%), and S (Alfa Aesar, 99.5%) and also following the same handling and heating profile as used for NaW_2S_4. Both samples were stored in an Ar-filled glovebox to prevent hydration. Both syntheses yielded 2H-WS_2 and did not appear to incorporate any of the Li, so they were repeated using twice the molar ratio of Li; these syntheses likewise yielded 2H-WS_2.

Preparation of K_xWS_2, 2M-WS_2, and 1T′-WS_2. The K_xWS_2 crystals were prepared via the method proposed by Song et al.[25] Likewise, 2M-WS_2 was prepared using the method by Song et al., with either NaW_2S_4 or Rb_xWS_2 used in place of K_xWS_2.[26] We used 0.02 M

https://doi.org/10.1021/acs.inorgchem.4c03350
Inorg. Chem. 2024, 63, 21954−21962

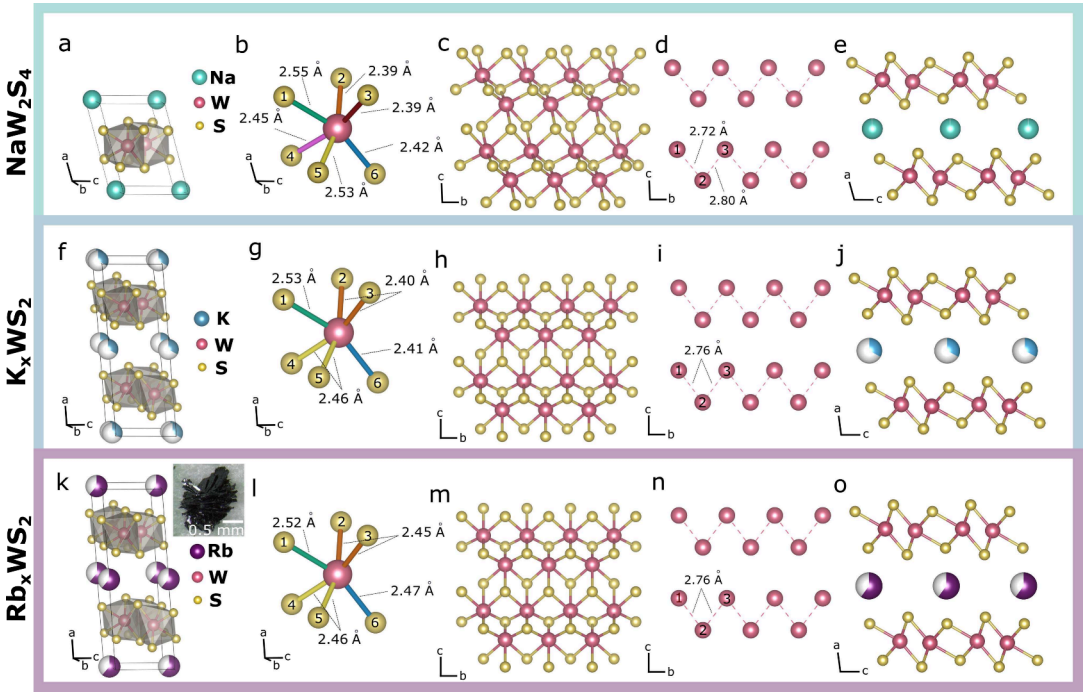

Figure 1. (a) Structure of NaW_2S_4 ($P\bar{1}$) showing a single unit cell of alternating layers of octahedrally coordinated $[WS_6]^{8-}$ and Na^+. (b) An enlarged view of $[WS_6]^{8-}$ highlights the different W−S bond lengths. Differing bond lengths are emphasized with different colors. (c) A view down the (100) plane shows a single layer of $[WS_2]^-$ and (d) its distorted zigzag W ions. (e) A view down the (010) plane shows the distinct layers of $[WS_2]^-$ and Na^+. (f−j) The same structural information is shown for the K_xWS_2 compound and (k−o) Rb_xWS_2. An inset of k shows the flower-like morphology that Rb_xWS_2 forms in. Refer to Table 1 for a comparison of the lattice parameters for each structure.

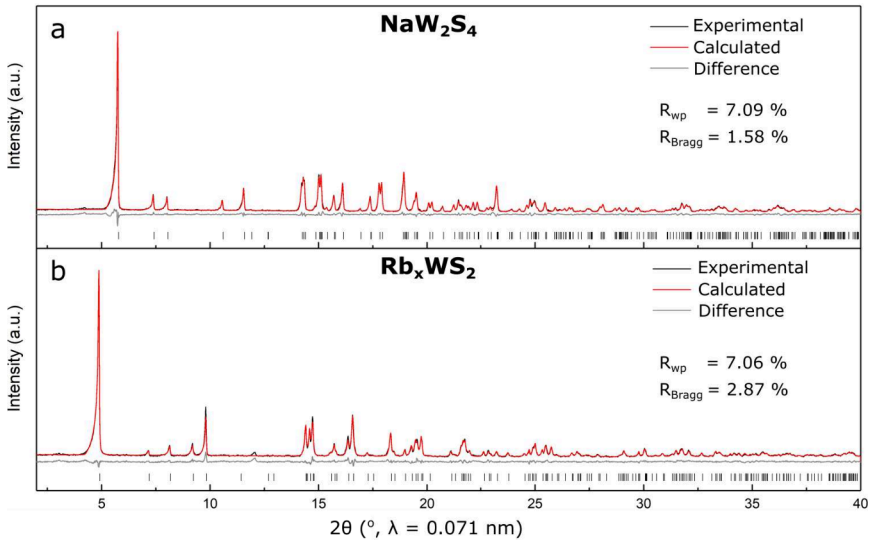

Figure 2. Rietveld refinement showing the calculated pattern in red, overlaying the acquired pattern in black and the difference in gray for (a) NaW_2S_4 and (b) Rb_xWS_2.

nitric acid to prepare the 2M-WS_2 since that had provided the best samples from K_xWS_2.[26] 1T′-WS_2 monolayers were made by exfoliating NaW_2S_4 or Rb_xWS_2 in sulfuric acid, following the procedure by Song et al.[25]

Materials Characterization. The bulk powder was analyzed with powder X-ray diffraction (PXRD) using a STOE STADI P X-ray diffractometer (Mo Kα1 radiation, Ge monochromator, Single-Mythen detector, Debye−Scherrer geometry). The Crystal structure was solved using TOPAS V7 (Bruker AXS).[33,34] Images and composition were taken using scanning emission spectroscopy (SEM) and energy dispersive X-ray diffraction (EDX), respectively, using a Quanta 200 FEG Environmental-SEM. Atomic resolution images and electron diffraction were taken with a Titan Cubed Themis 300 double Cs-corrected Scanning/Transmission Electron Microscope (HRSTEM). Fast Fourier Transform (FFT) patterns were calculated from HRSTEM images using ImageJ. A Magnetic Property Measurement System (MPMS3) from Quantum Design was used to obtain magnetic susceptibility on the resulting 2M-WS_2; a Physical Property Measurement System (PPMS Dynacool) from Quantum Design was used to obtain heat capacity data on the 2M-WS_2. A Bruker Dimension ICON3 Atomic Force Microscope (AFM) was used to measure the height of 1T′-WS_2 nanosheets. STEM and SAED images of 1T′-WS_2 nanosheets were obtained using a Talos F200X Scanning/Transmission Electron Microscope (S/TEM) and

https://doi.org/10.1021/acs.inorgchem.4c03350
Inorg. Chem. 2024, 63, 21954−21962

the structures of the sheets were confirmed with Raman spectroscopy using a Horiba Raman Spectrometer. An Agilent 5800 Inductively Coupled Plasma-Optical Emission Spectrometer (ICP-OES) was used to obtain exact atomic ratios.

RESULTS AND DISCUSSION

NaW_2S_4 and Rb_xWS_2 were prepared with solid-state methods, by combining their constituent elements and heating in a furnace (details in the Experimental Section). The NaW_2S_4 formed as a silver powder, whereas the Rb_xWS_2 appeared as black crystals with a flower-like morphology, which can be viewed in Figure 1k. The Rb_xWS_2 synthesis did not exclusively produce the desired product, however, the silvery crystals could be easily distinguished and separated from the powder impurities. The structures of NaW_2S_4 and Rb_xWS_2 are shown in Figure 1, where they can be compared with that of K_xWS_2. Additional solid-state syntheses were conducted in order to prepare Li_xWS_2, though each synthesis resulted in 2H-WS_2.

All characterization and experimentation were performed using the pure Rb_xWS_2 crystals. The structure solutions were performed on PXRD patterns for both NaW_2S_4 and Rb_xWS_2 (Figure 2) and refined with TOPAS V7 (Bruker AXS);[33,34] more information about the refinement can be found in the Supporting Information, SI. NaW_2S_4 was found to have a $P\bar{1}$ (No. 2) crystal structure. This is a slight distortion of the K_xWS_2 structure,[25] with similar b (3.300 Å) and c (5.704 Å) lattice parameters but an a (7.491 Å) parameter about half the size (Table 1). Unlike the K- and Rb-based structures, NaW_2S_4 refined with full occupancy of the Na ions, hence the doubled unit formula. Meanwhile, Rb_xWS_2 crystallizes with a $C2/m$ (No. 12) space group, which is the same as that of K_xWS_2. As with its K counterpart, the Rb sites are partially occupied, with $x \sim 0.3$. Rb_xWS_2 has similar b (3.271 Å) and c (5.699 Å) lattice parameters but an increased a (16.679 Å) parameter, with respect to K_xWS_2 (Table 1). This is expected, since Rb is larger than K, and thus, increases the interlayer spacing. A look at the interlayer spacing between layers of $[WS_2]^-$ shows a positive correlation with alkali metal size: Na (7.491 Å), K (8.074 Å), Rb (8.340 Å) (Table 2 and Table 3). Each of the three A_xWS_2 compounds consists of layers of distorted octahedrally coordinated $[WS_6]^{8-}$ separated by layers of alkali ions, illustrated in Figure 1e,j,o. Within the $[WS_6]^{8-}$ layers, the corresponding W−S bond lengths remain consistent regardless of the identity of A (Figure 1b,g,l and Table 3). It is interesting to note, however, that while S2 and S3, as well as S4 and S5, exhibit equal distances from their central W in the K and Rb compounds (Figure 1g,l and Table 3), all 6 of the W−S bond lengths for the Na compound are unique (Figure 1b and Table 3). We see further evidence of structural differences in the W zigzag chains along the b-axis; whereas the W−W distances are equal (W1−W2 = W2−W3) in K_xWS_2 and Rb_xWS_2, as shown in Figures 1h-i, m-n), the W zigzag chains in NaW_2S_4 are distorted (W1−W2 = 2.72 Å, W2−W3 = 2.80 Å) (Figure 1c,d). The W1−W2 distance in NaW_2S_4 is similar to the W−W bond length in W metal (2.74 Å), which may suggest W−W bonding, though further study would be needed to confirm the nature of this bonding.[35] Despite these differences, the W−W distances forming the chains of all three compounds are within 0.08 Å of each other, which highlights their similarities (Table 3).

To support the PXRD findings, high-resolution scanning transmission electron microscopy (HRSTEM) was conducted on a cross-section of NaW_2S_4 and Rb_xWS_2. As shown in Figure 3a, only the W ions are visible in the NaW_2S_4 cross-section. The distances between W ions intralayerally (d_1) and interlayerally (d_2) measured from the HRSTEM image match well with the corresponding distances measured based on the PXRD structure solution (Figure 3d). Likewise, the Fast Fourier Transform (FFT) pattern of the HRSTEM image matches well with that simulated from the structure file, as shown in Figure 3b,c. In Figure 3e, both the W atoms and Rb atoms are visible in the Rb_xWS_2 cross-section. The distances

Table 1. Lattice Parameters of NaW_2S_4, K_xWs_2, and Rb_xWS_2

	NaW_2S_4	K_xWS_2	Rb_xWS_2
side	length (Å)	length (Å)	length (Å)
a	7.4914(3)	16.15	16.6792(8)
b	3.3001(1)	3.259	3.2710(1)
c	5.7037(2)	5.685	5.6988(3)
vertice	angle (deg)	angle (deg)	angle (deg)
α	89.634(3)	90	90
β	105.704(2)	98.63	97.437(4)
γ	102.634(3)	90	90

Table 3. Bond Lengths within NaW_2S_4 and Rb_xWS_2

	NaW_2S_4	K_xWS_2	Rb_xWS_2
bond	distance (Å)	distance (Å)	distance (Å)
W−S1	2.553(9)	2.530	2.515(12)
W−S2	2.392(12)	2.399	2.449(9)
W−S3	2.393(10)	2.399	2.449(9)
W−S4	2.453(9)	2.460	2.456(8)
W−S5	2.534(10)	2.460	2.456(8)
W−S6	2.419(10)	2.406	2.468(13)
W1−W2	2.722(4)	2.758	2.761(3)
W1−W2	2.797(4)	2.758	2.761(3)
interlayer spacing	7.4914(3)	8.074	8.3396(4)

Table 2. Position Coordinates and Thermal Parameters for NaW_2S_4 and Rb_xWS_2

atom	x	y	z	occ.	Wyck	B_{eq}
Na	0	0.5	0	1	1c	4.0 (5)
W	−0.4896(3)	0.7478(8)	−0.6898(2)	1	2i	0.75(5)
S	−0.743(1)	0.638(4)	−0.493(2)	1	2i	1.10(19)
S	−0.685(1)	0.172(4)	−0.980(1)	1	2i	0.90(19)
Rb	0.5	0	1	0.58(1)	2a	4.0(5)
W	0.2461(2)	1	0.6933(3)	1	4c	0.37(6)
S	0.3582(7)	1	0.450(2)	1	4c	1.1(3)
S	0.3262(7)	0.5	0.946(2)	1	4c	0.2(2)

https://doi.org/10.1021/acs.inorgchem.4c03350
Inorg. Chem. 2024, 63, 21954−21962

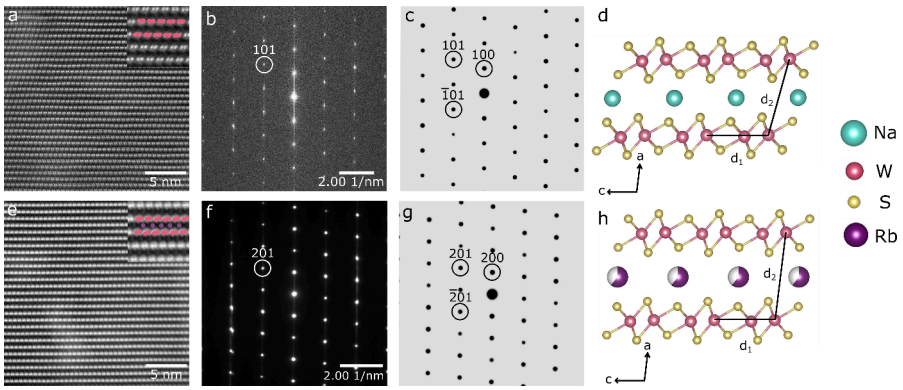

Figure 3. (a) HRSTEM of NaW_2S_4 looking down the (010) plane, showing distinct layers in the c-direction. A zoomed-in image of the HRSTEM is shown as an inset. (b) The FFT pattern of the HRSTEM compares well with (c) the expected electron diffraction. (d) The crystal structure from VESTA, viewed down at the (010) plane. (e) HRSTEM of Rb_xWS_2 looking down the (010) plane, showing distinct layers in the c-direction, as well as the Rb ions between the layers, which can be viewed more clearly in the zoomed-in inset. (f) The corresponding SAED compares well with (g) the expected electron diffraction. (h) The crystal structure from VESTA, viewed down at the (010) plane.

Table 4. d-Spacings of NaW_2S_4 and Rb_xWS_2

NaW_2S_4			Rb_xWS_2		
hkl	actual (Å^{-1})	simulated (Å^{-1})	hkl	actual (Å^{-1})	simulated (Å^{-1})
101	0.255	0.260	201	0.219	0.227
100	0.138	0.142	200	0.117	0.121
$\bar{1}$01	0.194	0.198	$\bar{2}$01	0.195	0.201
distance	actual (Å)	simulated (Å)	distance	actual (Å)	simulated (Å)
d_1	5.842	5.7037(2)	d_1	5.550	5.6988(3)
d_2	7.594	7.4914(3)	d_2	8.548	8.3396(4)

between W atoms intralayerally (d_1) and interlayerally (d_2) measured from the HRSTEM image match well with the corresponding distances from the structural solution (Figure 3h). Additionally, the Rb−Rb bond distances in the HRSTEM match those in the calculated structure. Likewise, the selected area electron diffraction (SAED) obtained from HRSTEM matches well with that simulated from the structure file, as shown in Figure 3f,g. Table 4 shows a comparison of the calculated and actual *d*-spacings and atomic distances for NaW_2S_4 and Rb_xWS_2.

Atomic fractions found with energy-dispersive X-ray spectroscopy (EDX) obtained from the high-resolution STEM agree with the PXRD refinements that are shown in Table 2. The Na content of NaW_2S_4 was found to be half that of W (Figure S1), which supports our finding of a unit formula of $Na_1W_2S_4$. Meanwhile, the Rb content of Rb_xWS_2 was found to be $x \sim 0.34$ and $x \sim 0.28$ from EDX and PXRD, respectively (Figure S2 and Table 2), similar to that of K_xWS_2, where $x \sim 0.33$.[25] This was further confirmed by EDX performed on a Scanning Emission Microscopy (SEM) instrument, which showed similar ratios (Figure S3 and SI Table S2). Contrast differences on the surface of the Rb_xWS_2 SEM image are likely from amorphous Rb_2S_2, which could account for slightly higher ratios of Rb and S compared to W (Figure S3b). This secondary phase does not show up in the PXRD, suggesting that it is amorphous. Furthermore, since it is a surface contamination and not part of the crystal, it does not show up in the HRSTEM EDX, which is imaged on a cross-section cut from the center of the crystal. Inductively coupled plasma-optical emission spectroscopy (ICP-OES) likewise agreed with the relative ratios and showed slightly higher amounts of Rb and S as compared with W (SI Table S3). Again, it is unsurprising that this excess material would be noticed in the ICP-OES, which indiscriminately characterizes the entire product.

To understand whether the new materials reported here are of use for quantum material synthesis, we tested them as starting materials for preparing 2M-WS_2 and 1T′-WS_2 monolayers (Figure 4). A schematic in Figure 5 illustrates the process of exfoliating NaW_2S_4 via sonication to form 1T-WS_2 and deintercalating NaW_2S_4 on a shaker to form 2M-WS_2. While NaW_2S_4 is portrayed in the diagram, the mechanism remains accurate with either K_xWS_2 or Rb_xWS_2 in its place. Both 2M-WS_2 and 1T′-WS_2 are structurally similar; each layer consists of edge-sharing $[WS_6]^{8-}$ with a distorted octahedral coordination. 2M-WS_2 refers to the bulk structure, which consists of two 1T′-WS_2 layers per unit cell.[36,37] As 2M-WS_2 is a highly studied material, for its potential to be a topological superconductor,[36] it is important to find reliable synthetic recipes for crystals of high quality. This is especially relevant for metastable materials, such as 2M-WS_2, as the necessary low-temperature methods are prone to introduce defects that cannot be removed by annealing. We previously had improved the established synthetic recipes of 2M-WS_2 by avoiding strong oxidizers that had been thought to be necessary for the reaction. It remains relevant to test if the choice of alkali intercalant in the starting materials can additionally positively affect the outcome of the superconducting synthetic product. In order to produce 2M-WS_2, we used dilute nitric acid to remove the respective alkali metals. We found that both the Na and Rb compounds as starting materials successfully produced 2M-WS_2. EDX shows these compounds to have about a 1:2 ratio of W to S (Figure S4, SI Table S4). While the Na took 48 h to deintercalate, similar to the K, the Rb only took 24 h; this

https://doi.org/10.1021/acs.inorgchem.4c03350
Inorg. Chem. 2024, 63, 21954−21962

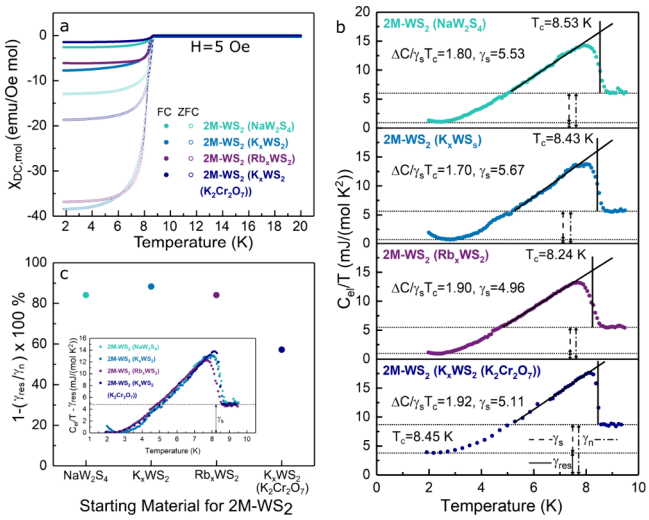

Figure 4. (a) Temperature-dependent magnetic susceptibility (χ) of 2M-WS_2 synthesized from NaW_2S_4 (green), Rb_xWS_2 (purple), K_xWS_2 (light blue), and K_xWS_2 ($K_2Cr_2O_7$) (dark blue) measured in H = 5 Oe in the FC state (closed circles) and ZFC state (open circles). The K_xWS_2 and K_xWS_2 ($K_2Cr_2O_7$) data are from ref 26. (b) Temperature dependent electronic heat capacity data scaled by temperature (C_{el}/T) for NaW_2S_4 (green), K_xWS_2 (light blue), Rb_xWS_2 (purple), and K_xWS_2 ($K_2Cr_2O_7$) (dark blue). See text for details. The data for K_xWS_2 ($K_2Cr_2O_7$) are from ref 26. (c) The superconducting volume fraction ($1 - \gamma_{res}/\gamma_n$) for NaW_2S_4 (green), K_xWS_2 (light blue), Rb_xWS_2 (purple), and K_xWS_2 ($K_2Cr_2O_7$) (dark blue). (Inset) The superconducting contribution to the specific heat $C_{el}/T - \gamma_{res}$ for NaW_2S_4 (green), K_xWS_2 (light blue), Rb_xWS_2 (purple), and K_xWS_2 ($K_2Cr_2O_7$) (dark blue).

may be due to the higher ion mobility of larger alkali ions. However, 2M-WS_2 from Rb_xWS_2 may contain a small impurity phase, indicated by peaks at ~18.2°, ~25.9°, ~ 31.8°, and ~36.9°. A Rietveld refinement that included a second, W, phase (space group $Im\bar{3}m$), indicated that this W impurity accounts for <2%. Additional time in acid, as required to fully remove Na^+ from NaW_2S_4 did not remove this second phase. Meanwhile, the 2M-WS_2 prepared from the NaW_2S_4 sample did not contain any impurity phase, according to the PXRD (Figure S5).

To test the superconducting properties, we measure the magnetic susceptibility, Figure 4a, of 2M-WS_2 synthesized from NaW_2S_4 (green) and Rb_xWS_2 (purple) and compare them to their counterparts synthesized previously in ref 26 from K_xWS_2 (light blue) and K_xWS_2 ($K_2Cr_2O_7$) (dark blue). The sharp diamagnetic transition in the field-cooled (FC) state confirms the superconductivity in all samples. The zero-field cooled (ZFC) susceptibility can be used to estimate the screening fraction of the sample; conversely, the FC curve can be used to estimate the superconducting volume fraction.[38] However, to perform this analysis, demagnetization effects must be taken into account. Vortex pinning, intrinsic to type-II superconductors, will further reduce the saturation value of the FC susceptibility.[39,40] Because our samples are pressed pellets, we expect there to be preferred orientation in the samples, especially the ones from K_xWS_2 and Rb_xWS_2, which are platelets, in which preferred orientation is severe, though it could vary from sample to sample, making it impossible to accurately account for demagnetization effects. Nonetheless, we note that 2M-WS_2 made from a strong oxidizer ($K_2Cr_2O_7$) exhibits a much reduced FC saturation value, reaching only, ~60%, ~25%, and ~20% of the FC saturation values of 2M-WS_2 made from NaW_2S_4, Rb_xWS_2, and K_xWS_2, respectively, supporting the idea that weak acids may be conducive to make 2M-WS_2 with higher superconducting volume fractions.

To gain a deeper understanding of the superconducting properties, we compare the heat capacity, C_p, between each sample. We measured the C_p from 2 to 9.5 K in H = 0 T and H = 5 T (well above the critical field) (see Figure S6). Above the superconducting transition, C_p measured at 0 and 5 T collapse onto each other. We, therefore, use the 5 T data as the normal state heat capacity C_n, which can be fit to $C_n = C_{el}^n + C_{ph} = \gamma_n T + \beta T^3 + \eta T^5$, as shown in Figure S6. Here, C_{el}^n is the electronic contribution to the normal state heat capacity, C_{ph} is the phonon contribution, γ_n is the coefficient of the electronic contribution, and β and η are the coefficients of the phonon contribution. Using the 5 T C_p data to subtract out the phonon contribution, we are then able to infer the superconducting electronic heat capacity, C_{el}, at H = 0 T, where C_{el} scaled by temperature C_{el}/T is plotted for the four samples in Figure 4b. A clear jump is noticeable at T_c for all four samples, consistent with the susceptibility measurements, where T_c is estimated to be the halfway point between $T(C_{el}/T = \gamma_n)$ and $T(C_{el}/T = C_{el}T(\max))$. The variation in T_c between the samples is less than 0.2 K.

Looking closer, it is apparent that C_{el}/T does not extrapolate to zero. Instead, the data exhibits saturation behavior, suggesting the presence of a nonsuperconducting volume fraction in all samples.[41] We denote the saturated value as γ_{res}, which we interpret as a contribution from the non-superconducting portion of the sample. Then, $\gamma_s = \gamma_n - \gamma_{res}$ represents the electronic specific heat coefficient in the normal state from only the superconducting portion of the samples, and $(1 - \gamma_{res}/\gamma_n) \times 100\%$, represents the superconducting

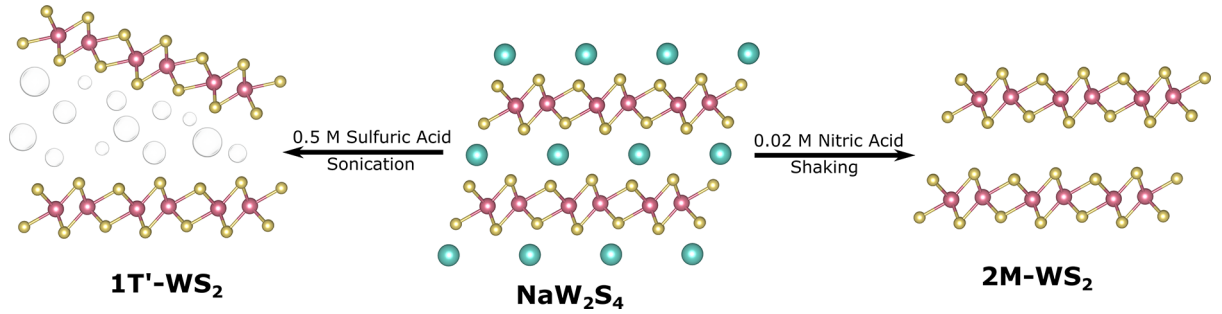

Figure 5. Schematic of the exfoliation of NaW_2S_4 into 1T′-WS_2 monolayers (left) and of the deintercalation of Na^+ from NaW_2S_4 to form 2M-WS_2 (right).

https://doi.org/10.1021/acs.inorgchem.4c03350
Inorg. Chem. 2024, 63, 21954−21962

volume fraction, which is plotted in the main panel of Figure 4c. Using this estimation of the superconducting volume fraction, the 2M-WS_2 samples made from NaW_2S_4 (green), Rb_xWS_2 (purple,) K_xWS_2 (light blue) using dilute nitric acid all have similar superconducting volume fractions, between ~82% to 85%. In contrast, the superconducting volume fraction for the sample made from K_xWS_2 with a strong oxidizer $K_2Cr_2O_7$ in dilute sulfuric acid (dark blue) yields a much smaller superconducting volume fraction ~58%.[26]

To compare the superconducting portions of the 2M-WS_2 samples synthesized from the different methods, we plot $C_{el}/T - \gamma_{res}$ in the inset of Figure 4c. Notably, within the scatter of the data, all samples have similar γ_s, indicating an intrinsic γ of 2M-WS_2. Furthermore, the data below T_c all collapse onto a single curve, indicating the gap structure is the same between all samples. Finally, the specific heat jump $\Delta C_{el}/(T_c\gamma_s)$ is greater than 1.43 and less than 3.7, consistent with BCS theory.[42] We note that a value of $\Delta C_{el}/(T_c\gamma_n) = 1.08$ was previously reported for 2M-WS_2 made from K_xWS_2 using $K_2Cr_2O_7$.[26] The discrepancy comes from γ_n being used in the previous calculation, which has contributions from the nonsuperconducting portion of the sample, greatly reducing $\Delta C_{el}/(T_c\gamma)$. Meanwhile, we isolated γ_s, the normal state electronic contribution, from only the superconducting volume fraction. With both methods, we draw the same conclusion, namely, 2M-WS_2 made from K_xWS_2 using $K_2Cr_2O_7$ makes samples with large nonsuperconducting volume fractions.

We find that, overall, the superconducting behavior of 2M-WS_2 prepared from each of the A_xWS_2 (A = Na, K, Rb) compounds is similar when using dilute nitric acid as the method of preparation. Furthermore, all three compounds were of higher quality than the one prepared with the strong oxidizer. We posit, then, that the method of alkali deintercalation is more consequential to the resulting product than the identity of the initial alkali-ion. We acknowledge that the jump in the specific heat of 2M-WS_2 prepared from the Rb-compound is not as sharp as that from the Na-compound. The broad transition of the former could result from the small W impurity or anisotropic behavior. As previously mentioned, the Rb_xWS_2 and, thus, the resulting 2M-WS_2, formed as large plate-like crystals. However, the superconducting volume fraction, estimated from the heat capacity, is consistent between the two samples. Therefore, while the inclusion of this W impurity and the geometry of the crystals may affect the appearance of the data, they do not diminish the quality of the product.

Finally, we tested NaW_2S_4 and Rb_xWS_2 as starting materials for preparing 1T′-WS_2 monolayers. Using dilute sulfuric acid and an ultrasonication bath, we found that monolayers could be easily prepared from both NaW_2S_4 and $RbWS_2$. Atomic Force Microscope (AFM) images in Figure 6 show the monolayers to be about 1 nm. Raman spectra (Figure S7a) confirm the phase to be 1T′, which is supported by SAED. STEM images of representative nanosheets can be seen in Figure S7b,c, which shows the typical lateral size of those prepared from NaW_2S_4 to be smaller (~2−4 μm) than those prepared from Rb_xWS_2 (~4−6 μm), possibly a consequence of the former being a powder versus platelets. Thus, by introducing NaW_2S_4 and Rb_xWS_2, we open the possibility for tunable sizes of monolayer 1T′-WS_2.

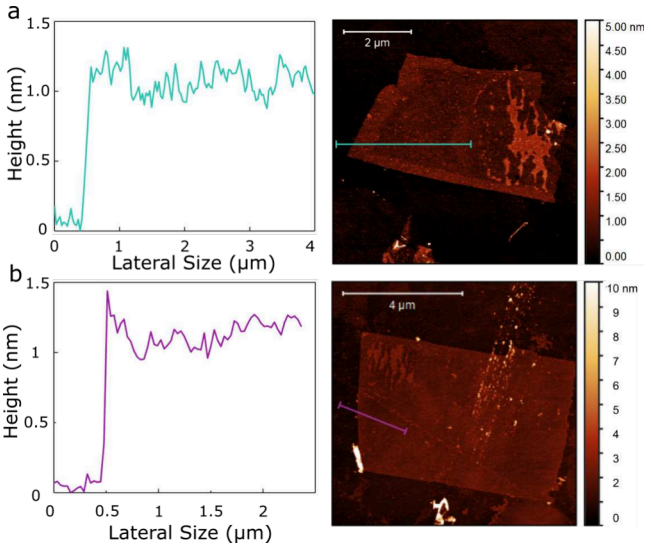

Figure 6. AFM of 1T′-WS_2 made by exfoliating (a) NaW_2S_4 and (b) Rb_xWS_2 in sulfuric acid.

CONCLUSIONS

We demonstrated a one-step solid-state synthesis for preparing two novel compounds: NaW_2S_4 and Rb_xWS_2. Unfortunately, attempts to synthesize Li_xWS_2 with solid-state methods, were unsuccessful. Using PXRD, we found these structures to have the space groups $P\bar{1}$ and $C2/m$, respectively. We note that the structure of NaW_2S_4 is a distorted version of that of Rb_xWS_2, as evidenced by the former's six unique W−S bond lengths in each $[WS_6]^{8-}$ and unequal W−W zigzag distances, as opposed to only four unique W−S bond lengths and equal W−W zigzag distances in the latter structure. Despite these differences, the two structures share similar lattice parameters and bond lengths with each other and with the previously prepared K_xWS_2. One noticeable difference is the increased interlayer spacing along the a-direction with each increasing size of alkali metal. We support these structural findings with HRSTEM images and electron diffraction patterns. Meanwhile, we confirm the atomic ratios with EDX from the SEM and STEM, and additional measurements with ICP-OES. We suspect that a slightly high ratio of alkali metal and sulfur may come from amorphous A_2S_2 in both compounds, which would explain why it is not seen in the PXRD. We next tested both compounds as starting materials for preparing 2M-WS_2 and found that, within error, both products showed similar superconducting behaviors. A comparison of 2M-WS_2 made from A_xWS_2 (A = Na, K, Rb) using dilute nitric acid, and from K_xWS_2 using $K_2Cr_2O_7$, suggests that the method of preparing 2M-WS_2 is far more consequential than the identity of A, on the resulting crystal's quality. Therefore, through this paper, we introduce two new layered compounds that can be substituted for K_xWS_2 in producing 2M-WS_2, thus, increasing the accessibility of the latter. Furthermore, as with the K_xWS_2, both NaW_2S_4 and Rb_xWS_2 can be successfully exfoliated into 1T′-WS_2 monolayers, increasing the attainability of superconducting 1T′-WS_2 ink.

https://doi.org/10.1021/acs.inorgchem.4c03350
Inorg. Chem. 2024, 63, 21954−21962

■ ASSOCIATED CONTENT

Supporting Information

The following files are available free of charge. The Supporting Information is available free of charge at https://pubs.acs.org/doi/10.1021/acs.inorgchem.4c03350.

Additional information on Structure solve and Rietveld refinement; EDX data from HRSTEM and SEM for NaW_2S_4 and Rb_xWS_2; elemental composition from ICP-OES; SEM and EDX data for 2M-WS_2; PXRD patterns for 2M-WS_2; additional heat capacity plots for 2M-WS_2; Raman, STEM, and SAED for 1T′-WS_2 (PDF)

Accession Codes

Deposition Numbers 2377140−2377141 contain the supplementary crystallographic data for this paper. These data can be obtained free of charge via the joint Cambridge Crystallographic Data Centre (CCDC) and Fachinformationszentrum Karlsruhe Access Structures service.

■ AUTHOR INFORMATION

Corresponding Author

Leslie M. Schoop − *Department of Chemistry, Princeton University, Princeton, New Jersey 08544, United States;* orcid.org/0000-0003-3459-4241; Email: lschoop@princeton.edu

Authors

Brianna L. Hoff − *Department of Chemistry, Princeton University, Princeton, New Jersey 08544, United States;* orcid.org/0000-0002-1971-8931

Grigorii Skorupskii − *Department of Chemistry, Princeton University, Princeton, New Jersey 08544, United States*

Jaime M. Moya − *Department of Chemistry, Princeton University, Princeton, New Jersey 08544, United States;* orcid.org/0000-0003-1241-9493

Fang Yuan − *Department of Chemistry, Princeton University, Princeton, New Jersey 08544, United States;* orcid.org/0000-0001-7286-3233

Guangming Cheng − *Princeton Materials Institute, Princeton, New Jersey 08544, United States;* orcid.org/0000-0001-5852-1341

Jiaze Xie − *Department of Chemistry, Princeton University, Princeton, New Jersey 08544, United States;* orcid.org/0000-0003-1813-9521

Nan Yao − *Princeton Materials Institute, Princeton, New Jersey 08544, United States;* orcid.org/0000-0002-4081-1495

Complete contact information is available at: https://pubs.acs.org/10.1021/acs.inorgchem.4c03350

Notes

The authors declare no competing financial interest.

■ ACKNOWLEDGMENTS

This research was supported by the DOD's Office for Naval Research (ONR), award number N00014-21-1-2733, the Gordon and Betty Moore foundation (EPIQS initiative), award number GBMF9064 and the Princeton Center for Complex Materials, a National Science Foundation (NSF)-MRSEC program (DMR-2011750). The authors acknowledge the use of Princeton's Imaging and Analysis Center, which is partially supported by the Princeton Center for Complex Materials, a National Science Foundation (NSF)-MRSEC program (DMR-2011750). B.L.H. is supported by the NSF Graduate Research Fellowship Program under grant number DGE-2039656. G.S. is supported by the Arnold and Mabel Beckman Foundation through his AOB Postdoctoral Fellowship (dx.doi.org/10.13039/100000997).

■ REFERENCES

(1) Mizushima, K.; Jones, P.; Wiseman, P.; Goodenough, J. B. Li_xCoO_2 ($0 < x < -1$): A new cathode material for batteries of high energy density. *Mater. Res. Bull.* **1980**, *15*, 783−789.

(2) Yabuuchi, N.; Yoshida, H.; Komaba, S. Crystal structures and electrode performance of alpha-$NaFeO_2$ for rechargeable sodium batteries. *Electrochemistry* **2012**, *80*, 716−719.

(3) Borg, C. K.; Zhou, X.; Eckberg, C.; Campbell, D. J.; Saha, S. R.; Paglione, J.; Rodriguez, E. E. Strong anisotropy in nearly ideal tetrahedral superconducting FeS single crystals. *Phys. Rev. B* **2016**, *93*, 094522.

(4) Freitas, D. C.; Weht, R.; Sulpice, A.; Remenyi, G.; Strobel, P.; Gay, F.; Marcus, J.; Núñez-Regueiro, M. Ferromagnetism in layered metastable 1T-$CrTe_2$. *J. Phys.: Condens. Matter* **2015**, *27*, 176002.

(5) Van Bruggen, C.; Haange, R.; Wiegers, G.; De Boer, D. $CrSe_2$, a new layered dichalcogenide. *Physica B+C* **1980**, *99*, 166−172.

(6) Song, X.; Schneider, S. N.; Cheng, G.; Khoury, J. F.; Jovanovic, M.; Yao, N.; Schoop, L. M. Kinetics and evolution of magnetism in soft-chemical synthesis of $CrSe_2$ from $KCrSe_2$. *Chem. Mater.* **2021**, *33*, 8070−8078.

(7) Kwon, K. D.; Refson, K.; Bone, S.; Qiao, R.; Yang, W.-l.; Liu, Z.; Sposito, G. Magnetic ordering in tetragonal FeS: Evidence for strong itinerant spin fluctuations. *Phys. Rev. B* **2011**, *83*, 064402.

(8) Sines, I. T.; Vaughn II, D. D.; Misra, R.; Popczun, E. J.; Schaak, R. E. Synthesis of tetragonal mackinawite-type FeS nanosheets by solvothermal crystallization. *J. Solid State Chem.* **2012**, *196*, 17−20.

(9) Zeng, S.-L.; Wang, H.-X.; Dong, C. Synthesis and electrical conductivity of nanocrystalline tetragonal FeS. *Chinese Physics B* **2014**, *23*, 087203.

(10) Lai, X.; Zhang, H.; Wang, Y.; Wang, X.; Zhang, X.; Lin, J.; Huang, F. Observation of superconductivity in tetragonal FeS. *J. Am. Chem. Soc.* **2015**, *137*, 10148−10151.

(11) Shi, Y.; Li, J.; Yu, H.; Zhou, Y.; Zhang, H.; Dong, C. Structural and physical properties of the $Na_xCoO_2 \cdot yH_2O$ superconducting system. *Supercond. Sci. Technol.* **2004**, *17*, 42.

(12) Schaak, R.; Klimczuk, T.; Foo, M. L.; Cava, R. Superconductivity phase diagram of $Na_xCoO_2{\cdot}1.3H_2O$. *Nature* **2003**, *424*, 527−529.

(13) Omomo, Y.; Sasaki, T.; Wang; Watanabe, M. Redoxable nanosheet crystallites of MnO_2 derived via delamination of a layered manganese oxide. *J. Am. Chem. Soc.* **2003**, *125*, 3568−3575.

(14) Yang, M.; Cheng, G.; Mathur, N.; Singha, R.; Yuan, F.; Yao, N.; Schoop, L. M. Chemical exfoliation of 1-dimensional antiferromagnetic nanoribbons from a non-van der Waals material. *Nanoscale Horiz.* **2024**, *9*, 479.

(15) Ko, D.-S.; Lee, W.-J.; Sul, S.; Jung, C.; Yun, D.-J.; Kim, H.-G.; Son, W.-J.; Chung, J. G.; Jung, D. W.; Kim, S. Y.; et al. Understanding the structural, electrical, and optical properties of monolayer h-phase RuO_2 nanosheets: a combined experimental and computational study. *NPG Asia Materials* **2018**, *10*, 266−276.

(16) Weber, D.; Schoop, L. M.; Wurmbrand, D.; Laha, S.; Podjaski, F.; Duppel, V.; Müller, K.; Starke, U.; Lotsch, B. V. IrOOH nanosheets as acid stable electrocatalysts for the oxygen evolution reaction. *Journal of materials chemistry A* **2018**, *6*, 21558−21566.

(17) Ma, R.; Sasaki, T. Two-dimensional oxide and hydroxide nanosheets: controllable high-quality exfoliation, molecular assembly, and exploration of functionality. *Accounts of chemical research* **2015**, *48*, 136−143.

(18) Tsiamtsouri, M. A.; Allan, P. K.; Pell, A. J.; Stratford, J. M.; Kim, G.; Kerber, R. N.; Magusin, P. C.; Jefferson, D. A.; Grey, C. P. Exfoliation of layered Na-ion anode material $Na_2Ti_3O_7$ for enhanced capacity and cyclability. *Chem. Mater.* **2018**, *30*, 1505−1516.

(19) Masuda, Y.; Hamada, Y.; Seo, W. S.; Koumoto, K. Exfoliation of layers in Na_xCoO_2. *J. Nanosci. Nanotechnol.* **2006**, *6*, 1632−1638.
(20) You, W.; Xiang, K. Controllable synthesis of ultrathin monolayer titanate nanosheet via osmotic swelling to exfoliation of layered titanate. *Ceram. Int.* **2021**, *47*, 19169−19179.
(21) Zheng, J.; Zhang, H.; Dong, S.; Liu, Y.; Tai Nai, C.; Suk Shin, H.; Young Jeong, H.; Liu, B.; Ping Loh, K. High yield exfoliation of two-dimensional chalcogenides using sodium naphthalenide. *Nat. Commun.* **2014**, *5*, 2995.
(22) Joensen, P.; Frindt, R.; Morrison, S. R. Single-layer MoS_2. *Materials research bulletin* **1986**, *21*, 457−461.
(23) Weber, D.; Schoop, L. M.; Duppel, V.; Lippmann, J. M.; Nuss, J.; Lotsch, B. V. Magnetic properties of restacked 2D spin 1/2 honeycomb $RuCl_3$ nanosheets. *Nano Lett.* **2016**, *16*, 3578−3584.
(24) Wang, L.; Fang, Y. YQ; Huang, f.; Cheng, E.; Ni, J.; Pan, B.; Xu, Y.; Huang, F.; Li, S. Nodeless superconducting gap in the topological superconductor candidate 2M-WS_2. *Phys. Rev. B* **2020**, *102*, 024523.
(25) Song, X.; Singha, R.; Cheng, G.; Yeh, Y.-W.; Kamm, F.; Khoury, J. F.; Hoff, B. L.; Stiles, J. W.; Pielnhofer, F.; Batson, P. E.; Yao, N.; Schoop, L. M. Synthesis of an aqueous, air-stable, superconducting 1T'-WS_2 monolayer ink. *Sci. Adv.* **2023**, *9*, eadd6167.
(26) Song, X.; Hoff, B.; Singha, R.; Stiles, J. W.; Skorupskii, G.; Khoury, J. F.; Cheng, G.; Kamm, F.; Uzan, A. J.; Dulovic, S.; et al. Acid-assisted soft chemical route for preparing high-quality superconducting 2M-WS_2. *Chem. Mater.* **2023**, *35*, 5487−5496.
(27) Zhao, C.; Che, X.; Fang, Y.; Liu, X.; Huang, F. Suppression of the superconducting transition temperature in Se-doping 2M-WS_2. *J. Phys. Chem. Solids* **2021**, *149*, 109789.
(28) Li, Y. W.; Zheng, H. J.; Fang, Y. Q.; Zhang, D. Q.; Chen, Y. J.; Chen, C.; Liang, A. J.; Shi, W. J.; Pei, D.; Xu, L. X.; Liu, S.; Pan, J.; Lu, D. H.; Hashimoto, M.; Barinov, A.; Jung, S. W.; Cacho, C.; Wang, M. X.; He, Y.; Fu, L.; Zhang, H. J.; Huang, F. Q.; Yang, L. X.; Liu, Z. K.; Chen, Y. L. Observation of topological superconductivity in a stoichiometric transition metal dichalcogenide 2M-WS_2. *Nat. Commun.* **2021**, *12*, 2874.
(29) Kaufman, J. L.; Vinckeviciute, J.; Krishna Kolli, S.; Gabriel Goiri, J.; Van der Ven, A. Understanding intercalation compounds for sodium-ion batteries and beyond. *Phil. Trans. R. Soc. A* **2019**, *377*, 20190020.
(30) Yohannan, J. P.; Vidyasagar, K. Syntheses, structural variants and characterization of $AInMS_4$ (A= alkali metals, Tl; M= Ge, Sn) compounds; facile ion-exchange reactions of layered $NaInSnS_4$ and $KInSnS_4$ compounds. *J. Solid State Chem.* **2016**, *238*, 291−302.
(31) Friedrich, D.; Hao, S.; Patel, S.; Wolverton, C.; Kanatzidis, M. G. Vast Structural and Polymorphic Varieties of Semiconductors $AMMQ_4$ (A= K, Rb, Cs, Tl; M= Ga, In; M= Ge, Sn; Q = S, Se). *Chem. Mater.* **2021**, *33*, 6572−6583.
(32) Mao, Y.; Fang, Y.; Wang, D.; Bu, K.; Wang, S.; Zhao, W.; Huang, F. Crystal structure and electrical resistance property of $Rb_{0.21}(H_2O)_yWS_2$. *Acta Crystallographica Section E: Crystallographic Communications* **2019**, *75*, 976−979.
(33) Perl, J.; Shin, J.; Schümann, J.; Faddegon, B.; Paganetti, H. TOPAS: an innovative proton Monte Carlo platform for research and clinical applications. *Medical physics* **2012**, *39*, 6818−6837.
(34) Faddegon, B.; Ramos-Méndez, J.; Schuemann, J.; McNamara, A.; Shin, J.; Perl, J.; Paganetti, H. The TOPAS tool for particle simulation, a Monte Carlo simulation tool for physics, biology and clinical research. *Physica Medica* **2020**, *72*, 114−121.
(35) Deshpande, V.; Pawar, R. X-ray determination of the thermal expansion of tungsten. *Curr. Sci.* **1962**, *31*, 497−499.
(36) Fang, Y.; Pan, J.; Zhang, D.; Wang, D.; Hirose, H. T.; Terashima, T.; Uji, S.; Yuan, Y.; Li, W.; Tian, Z.; Xue, J.; Ma, Y.; Zhao, W.; Xue, Q.; Mu, G.; Zhang, H.; Huang, F. Discovery of superconductivity in 2M-WS_2 with possible topological surface states. *Adv. Mater.* **2019**, *31*, 1901942.
(37) Liu, X.; Zhang, P.; Wang, S.; Fang, Y.; Wu, P.; Xiang, Y.; Chen, J.; Zhao, C.; Zhang, X.; Zhao, W.; Wang, J.; Huang, F.; Guan, C. High intrinsic phase stability of ultrathin 2M WS2. *Nat. Commun.* **2024**, *15*, 1263.
(38) Devarakonda, A.; Inoue, H.; Fang, S.; Ozsoy-Keskinbora, C.; Suzuki, T.; Kriener, M.; Fu, L.; Kaxiras, E.; Bell, D. C.; Checkelsky, J. G. Clean 2D superconductivity in a bulk van der Waals superlattice. *Science* **2020**, *370*, 231−236.
(39) Bean, C. P. Magnetization of hard superconductors. *Physical review letters* **1962**, *8*, 250.
(40) Goldfarb, R. B.; Lelental, M.; Thompson, C. *Alternating-Field Susceptometry and Magnetic Susceptibility of Superconductors*; Springer: Berlin/Heidelberg, 1991.
(41) Asaba, T.; Lawson, B. J.; Tinsman, C.; Chen, L.; Corbae, P.; Li, G.; Qiu, Y.; Hor, Y. S.; Fu, L.; Li, L. et al. Rotational Symmetry Breaking in a Trigonal Superconductor Nb-doped Bi_2Se_3. *Phys. Rev. X* **2017**, *7* DOI: 10.1103/PhysRevX.7.011009.
(42) Tari, A. *The Specific Heat of Matter at Low Temperatures*; World Scientific: Singapore, 2003.

https://doi.org/10.1021/acs.inorgchem.4c03350
Inorg. Chem. 2024, 63, 21954−21962